Powder bed fusion on single lines of Cu-doped hydroxyapatite powder bed

François Rouzé l'Alzit, Benoit Glorieux, Thierry Cardinal, Manuel Gaudon

Materials & Design 252 (2025) 113757

Contents lists available at ScienceDirect

Materials & Design

journal homepage: www.elsevier.com/locate/matdes

Powder bed fusion on single lines of Cu-doped hydroxyapatite powder bed

François Rouzé l'Alzit, Benoit Glorieux, Thierry Cardinal, Manuel Gaudon *

Institut de Chimie de la Matière Condensée de Bordeaux, UMR5026, CNRS, 87 avenue du Dr. A. Schweitzer, 33608 Pessac, Cedex, France

ARTICLE INFO

Keywords:
Powder bed fusion
Hydroxyapatite
Thermal gradients
Ceramics

ABSTRACT

This study aims to design ceramic scaffolds for precise bone reconstruction using Powder Bed Laser Sintering (PBLS) to create cohesive Cu-doped HAp ribbons from a single lasered line on a thin powder bed atop a silicate lime substrate. Depending on laser parameters, two ribbon types—delaminated (CDR) or anchored (CAR)—are produced, both exhibiting surface density gradients from the center to the edges. Microscale analysis reveals surface density gradients in both ribbon types, extending from center to edge. CDRs also show depth-wise density variations, resulting in mechanical stresses that cause detachment and curling. In CARs, intense local heating and thermal conductivity cause a temperature rise beyond the irradiated area. The substrate acts as a thermal barrier, concentrating heat at the film-substrate interface and ensuring ribbon adhesion. Cracks propagate perpendicular to isothermal lines, enabling controlled crack patterning.

1. Introduction

Bone tissue continuously regenerates, repairing fractures naturally. However, severe injuries may require bone grafts. Ceramic implants, especially calcium phosphates, are popular in bone regeneration due to their biocompatibility, osseointegration, and osteoconduction [1,2]. These porous implants facilitate new bone tissue growth.

Hydroxyapatite (HAp), $Ca_{10}(PO_4)_6(OH)_2$, is the primary inorganic component in bone (≈60 wt%) and dental enamel (90 wt%). Its nanometric form exhibits excellent biocompatibility and osteoconduction [3–5]. HAp's hexagonal structure allows for various ion substitutions of Ca^{2+}, P^{5+}, PO_4^{3-} or OH^- ions, enhancing its versatility for biomedical applications. HAp's ion substitution capacity allows modification of biological responses [6]. Naturally occurring elements in the body, like silicon, copper, and iron, can be incorporated into the HAp structure [7]. Incorporating elements like copper into HAp can enhance antibacterial properties, stimulate blood vessel growth, and accelerate bone regeneration [8]. This improves the mechanical integrity and antibacterial efficacy of biomedical coatings [9,10].

Bone substitutes must match the patient's anatomy and mimic bone architecture. Additive manufacturing (AM) enables the creation of customized [11–16], complex structures tailored to the patient's morphology, making it increasingly valuable in biomedical applications [17–24]. Optimal bone reconstruction scaffolds feature a woodpile design with overlapping rods, spaced about half a millimeter apart, and arranged in perpendicular layers. Mastering the production of elementary "ribbon" structures is crucial for creating woodpile-like scaffolds. These designs promote neovascularization and optimize bone growth [4]. Additive manufacturing enables complex structures that overcome limitations of traditional methods [25].

Powder bed laser sintering (PBLS), also named powder bed fusion [25], is one of AM technique that is showing real interest, particularly in the medical field [26]. However, manufacturing ceramics scaffolds using the selective laser sintering technique is a challenge due to their high melting point, their absence or low plasticity and their poor resistance to thermal shock. In addition, ceramics have low absorptivity in the visible and near infrared [25,27]. In order to achieve powder bed laser sintering, it therefore appears necessary to optimize the material and laser parameters [28].

Depending on the shaped materials, two laser sintering methods are used [29]. On the one hand, the indirect method including a base material consisting of the ceramic phase mixed with a sacrificial polymer binder. Due to the lower melting point than the ceramic phase, the polymer binder melts and binds the ceramic particles together under laser beam to form a cohesive part [30–33]. In general, as with stereolithography, post-processing techniques are used to remove the polymer binder and then densify the ceramic by solid state sintering. The polymer can sometimes also be retained within the final part, depending on the specifications imposed. Among the biocompatible polymers used are polyetheretherketone (PEEK) [34,35], polyamides [36,37] and polycaprolactone (PCL) [38,39].

The direct method sinters or fuses ceramic material without a

* Corresponding author.
E-mail address: manuel.gaudon@icmcb.cnrs.fr (M. Gaudon).

https://doi.org/10.1016/j.matdes.2025.113757
Received 4 September 2024; Received in revised form 28 January 2025; Accepted 21 February 2025
Available online 22 February 2025

sacrificial binder to achieve the desired shape. Post-processing may be used for further densification. In 2007, Bertrand et al. [40] demonstrated PBLS could produce coherent zirconia parts, but with inadequate density and mechanical properties. Shuai et al. [41–43] recently demonstrated direct laser sintering of nanometric HAp using a CO2 laser. By optimizing laser parameters, they successfully created objects from nano-HAp powder. However, the mechanical properties of these parts remain significantly inferior to conventionally sintered ceramics.

To enhance direct ceramic sintering, absorption doping ions can be added to improve laser absorption. These ions, selected for high absorptivity at the laser wavelength, can also be biocompatible, biodegradable, soluble, or heat-degradable [29]. Anastasiou et al. [44] found that pure HAp showed no sintering or phase changes during laser interaction, while iron-doped HAp exhibited characteristics of a sintered material, as revealed by X-ray diffraction analysis.

In our previous publications [45,46], we studied the laser sintering of copper-doped HAp. Copper was used for antibacterial and angiogenic properties. Integrating the Cu^{+} ions into the HAp matrix modifies the material's absorption properties (with pink coloration) at the laser wavelength (Fig. 1**a**). The powder obtained was then finely ground to obtain micrometric particles (Fig. 1**b**). Films of controlled thickness are obtained by dip-coating (Fig. 1**c**). Laser sintering is then used to produce partially sintered ribbons of material as a function of specific laser power/scanning speed/focusing regimes. A deeper investigation at the micrometer scale would allow a finer experimental assessment of the thermal processes that occur within the powder bed and the impact of different parameters (laser or materials).

The combination of laser parameters (power, scanning speed, and focusing) controls the energy delivered to the material. Detailed investigation of these parameters provided insights into the effects of lasering on Cu-doped HAp films, including crack formation and layer delamination, resulting from high temperatures and steep temperature gradients [46]. Laser power and scanning speed are interdependent parameters that determine the energy transferred to the powder bed. Lower scanning speeds typically result in better material cohesion and denser structures [25]. While low scanning speeds improve cohesion, excessively slow speeds can cause overheating, leading to imperfections and reduced functionality [47]. Laser power modulation produces similar effects to speed adjustment, but with a greater impact on density and mechanical properties, as demonstrated by Beal et al [48].

Focal length is another crucial laser parameter for controlling sintering [49,50]. Defocusing the laser reduces peak temperatures and thermal gradient steepness [51] while increasing spot diameter, resulting in more homogeneous sintering near the beam spot. We recently showed that defocusing reduces thermal gradients by increasing lasering time as the spot diameter grows [52]. Combined with low speed, it extends laser-powder contact time, helping moderate thermal gradients and reduce cracks [53]. Defocusing is thus a key parameter for controlling beam intensity during material interaction [54].

Previous tests [45] demonstrated that cohesive Cu-doped HAp ribbons, similar in size to alveolar bone trabeculae, could be formed by direct laser sintering using specific parameters (Fig. 1**d,f,e**). This study aims to understand and control the thermal gradients that enable ribbon formation. This study examines how Cu-doped HAp properties (film absorption coefficient and thickness) and laser parameters (power, focusing, and writing speed) affect temperature distribution in and around the irradiated area, including post-irradiation evolution. This understanding is crucial for developing scaffolds for biomedical applications.

2. Experimental

2.1. Powder preparation

A quantity of copper oxide (II) was mixed to the HAp powder (Sigma-Aldrich) to obtain a copper concentration x = 0.1 in the formula $Ca_{10}Cu_x(PO_4)_6O_{2x}(OH)_{(2-2x)}$. The HAp-CuO powder mixture was crushed by attrition to reduce particle size and further promote solid-state reaction. Attrition was performed in a 100 mL Teflon bowl in the presence of approximately 50 mL of distilled water, 1 wt% Darvan CN dispersant and 75 g yttrium-stabilized zirconia balls of 1 mm diameter. Attrition speed of 800 rpm was applied for 3 h. The suspension was dried

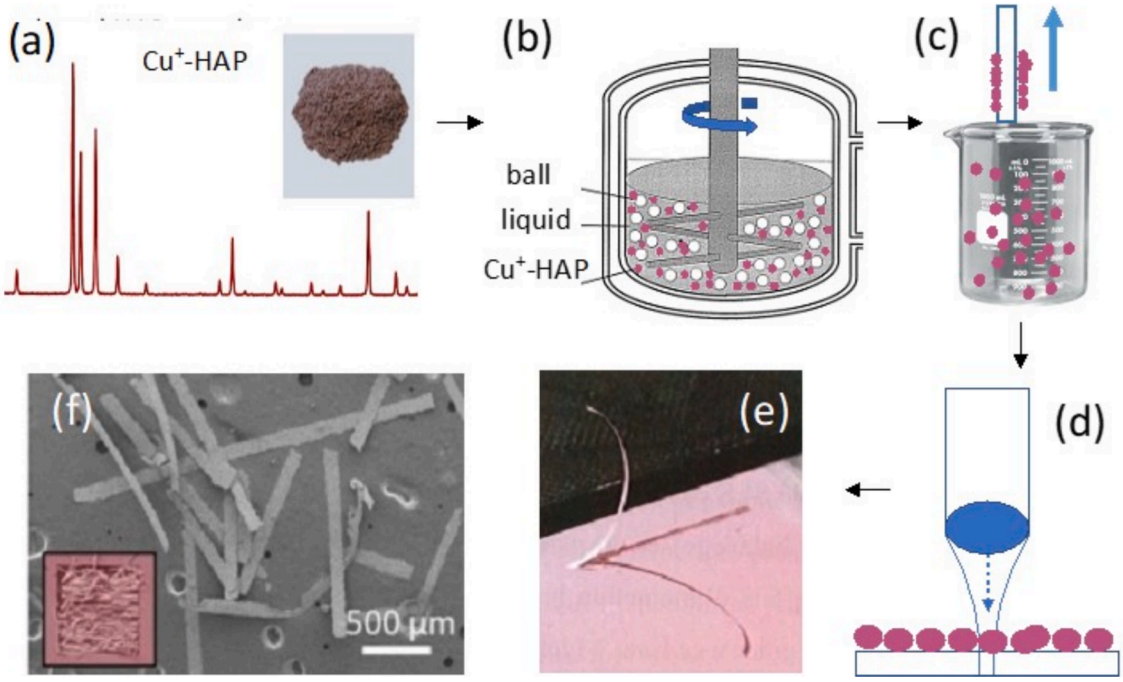

Fig. 1. Process of fabrication of ceramic ribbons. (a) The X-ray diffraction pattern and the pink color of the Cu-doped HAp powder obtained from synthesis route describes elsewhere [45], (b) attrition process of the powder predisposed in ethanol suspension in zirconia balls & jar, (c) dip-coating on glass substrate of the attrited suspension, (d) high-powder lasing of the Cu-doped HAp films, (e) photographs and (f) SEM micrographs of the HAp ribbons.

in an oven at 100 °C. The resulting powder were pressed into pellets of 10 mm diameter by applying a uniaxial pressure of 100 MPa. Finally, the pellets were calcined (ramp 10 °C/min) for 1 h at a temperature of 1100 °C to obtain a pure Cu^{+}-doped HA phase [46,47].

2.2. Thin films preparation

The resulting pellets from powder synthesis were firstly re-crushed in a 100 mL Teflon bowl in the presence of approximately 50 mL of ethanol, 2 wt% Beycostat C213 dispersant and 75 g of yttrium-stabilized zirconia balls, with an attrition speed of 800 rpm for 6 h. After separation from the zirconia balls, the suspension contained 30 wt% of Cu-doped HA powder and was then used for film deposition by dip-coating. The dip-coating method was used to coat a silicate glass substrate with a drawing speed of 400 mm/min. 5 successive layers were deposited, with a drying step of the as-prepared film at 100 °C for 15 sec between each coating step, to obtain 12 μm film thickness.

2.3. Powder and film characterization

Powder or film X-ray diffraction (XRD) patterns were recorded on a PANalitycal X'pert PRO MPD diffractometer in Bragg-Brentano θ-θ geometry equipped with a secondary monochromator and X'Celerator multi-strip detector. Each measurement was made within an angular range of 2θ = 8-80° a 0.017°-step scan rate and a counting time of 59 s. The Cu-Kα radiation was generated at 45 kV and 40 mA (λ = 0.15418 nm).

The UV–visible-NIR powder absorption spectra were measured with a double-beam spectrophotometer (CARY 5000 UV–vis–NIR) over the 250–2500 nm spectral region.

SEM investigations were performed using a JEOL JSM-67 in electron back-scattering mode.

2.4. Powder bed laser sintering facilities

The laser machine used for the experimentation was a continuous ytterbium fiber laser with an emission wavelength of 1.070 μm, which has been especially designed according to the laboratory specifications by ES Laser (ES17-355). This equipment has a focal distance of 199 mm, a spot size ∅ = 40 μm and its maximum and minimum operating power is 400 W and 40 W respectively. Experiments were carried out in air, using thin films on glass substrates as samples on a fixed sample stage. The 3 modulating parameters used in the experiments are the power (expressed as a % of maximum power), the scanning speed (in m/s) and the focus height (in mm). The defocusing was performed by moving the laser backwards in relation to the surface of the sample, i.e. with a focus point at a z distance above the surface of the material.

2.5. Numerical simulation equations

The numerical solution of the 2D transient heat equation has been achieved using the FlexPDE Multiphysics Finite Element solver (FlexPDE Lite v7.16, https://www.pdesolutions.com), details of which are reported elsewhere [46]. The modelling approach is focused on heat transfer from the laser to the film and from the film to its environment. It does not consider single particles but treats instead the powder film as a continuum with homogenized properties. Moreover, since the film thickness *d* is much smaller than the other dimensions, it is chosen to restrict the model to a 2D depth–averaged model.

3. Results and discussions

3.1. Preliminary studies

The first experiments were carried out on Cu^{+}-doped HAp films with a perfectly focused laser, power set at 40 W for variable lasering speeds (Fig. 2).

Regarding the results, 3 speed ranges could be identified. Firstly, at fast speeds (higher than of 40 mm/s), the films are only slightly affected by the laser. The energies transmitted by the radiation-matter interaction to the powder beds are then too low. The temperatures reached do not allow consolidation of the lasered line. Secondly, at very low speeds (below 10 mm/s), the lasered lines are clearly visible, with a slightly different coloration to the non-lased parts. These lines show a certain transparency (transmission turbidity), whereas the non-lased film is perfectly opaque. This semi-transparency reflects the high densification of the lasered lines under the effect of advanced sintering, made possible by the high energy transfer from the radiation to the powder bed. However, the lines remain anchored to the substrate. Finally, for an intermediate speed range, the lasered segments peel away from the substrate, partially rolling up on themselves to form curved, mechanically cohesive ribbons that can be handled as a single unit. These ribbons are therefore enough sintered to have consolidated the powder bed into a ceramic object. A more detailed study of the effects of scanning speed around the speed ranges, established that the limiting speeds for obtaining debonded ribbons ranged from s = 15 mm/s to 40 mm/s (Fig. 2**b,2c**). For a well-targeted range of laser parameters, it is possible to obtain cohesive ribbons that are independent of the substrate. As previously evidenced, the lines obtained at lower scanning speeds, having received more energy and therefore greater consolidation, remain anchored to the substrate. One of the first studies undertaken in these intermediate and low speed ranges was to vary the laser's focus in order to control the width of the lasered lines. By modifying the focus, not only the surface power at the laser spot, but also the spatial distribution of temperature gradients and the time taken for a point on the film to pass through the laser (and therefore the temporal temperature gradients) are all affected.

As the laser beam has a Gaussian spatial distribution, the radius of

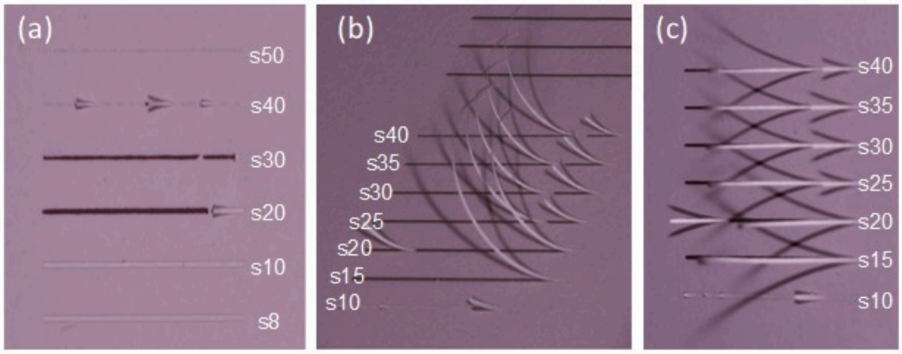

Fig. 2. Powder bed fusion process on the Cu-doped HAP thin films with (a) laser speed from 8 to 50 mm/sec[1], (b) and (c) laser speed from 10 to 40 mm/sec[1].

the sport size is conventionally W_z, which is defined as the point where the irradiance is $1/e^2$ (13.5 %) of its maximum value [52]. Beam focus is governed on our experimental setup as the height z (in mm) of the laser source taken with respect to the reference height (z = 0 mm/∅ spot = 40 μm) for optimized focus on the surface of the powder bed. As shown in Fig. 3, the $2w_z$ diameter of the laser sport on the surface of the powder bed increases from 100.0 μm for z = 0 (∅ spot = 40 μm) to 350 μm about for z = 4 mm (∅ spot = 140 μm).

Spatial thermal gradients are greatly affected by focusing. The temperature (relative temperature over the room temperature) on a line perpendicular to the lasered line passing through the beam spot can be simulated using FlexPDE thermal modelling software [46]. The temperature curves obtained for various défocalisation heights are shown in Fig. 3**c**. At the centre of the lasered line, the temperature reached is as approximately halved between z = 0/∅ spot = 40 μm and z = 4 mm/∅ spot = 140 μm, and halved again between z = 4/∅ spot = 140 μm mm and z = 12 mm/∅ spot = 400 μm. The greater spread of the irradiation spot, with an increase in the height of the laser source, means that at a distance of 200 μm from the centre of the line, the temperature reached is twice as high for z = 12 mm/∅ spot = 400 μm as for z = 4 mm/∅ spot = 140 μm (the temperature at this distance from the centre of the lasered line remains the room temperature).

Then, studies in this publication focuses on structural analyses of the effects of irradiation of a powder bed on the surface of lasered lines, whether they are detached as cohesive ceramic delaminated ribbons (CDR) or remain anchored to the substrate and named ceramic anchored ribbons (CAR). Lastly, we'll take a look at the density gradients "in depth", based on cross-sectional views of objects obtained after laser heating.

3.2. Effects of irradiation on surface

3.2.1. Ceramic delaminated ribbons (CDR)

The four CDRs from two different defocusing heights (z = 0/∅ spot = 40 μm and z = 6 mm/∅ spot = 200 μm) and for two scanning speeds of 15 and 40 mm/s are compared (Fig. 4) using SEM micrographs.

Whatever the CDR studied, the micrographs show CDR with sharp edges. Regarding the smooth shape of the thermal gradient (Fig. 3), a critical temperature at which mechanical cohesion by grain bonding is possible is evidenced.

Comparison of the two CDRs sets obtained with z = 0 mm/∅ spot = 40 μm or using z = 6 mm/∅ spot = 200 μm focal height, two parameter sets with quite same deposited energy but leading to different regimes, shows that real control over the width of these CDRs is performed by adjusting the distance between laser and powder bed. In agreement with the modelling of the laser as a Gaussian beam (see Fig. 3), the CDRs with z = 0 mm/∅ spot = 40 μm are around sixty microns wide, whereas those obtained with z = 6 mm/∅ spot = 200 μm are three time as wide. Furthermore, and especially for lasered CDRs with a laser scanning speed: s = 15 mm/s, a density gradient from the core to the CDR edges can be clearly distinguished, with larger grain sizes, wider sinter necks between them and a higher total density in the centre of the CDR compared with the edges.

We then conducted a study to obtain the widest possible CDRs, the first action is to defocus the laser. However, the temperatures reached by energy transfer tend to decrease as a result of the lower power density received by the sample. To maintain well-defined CDR, the laser power must be increased, or the scanning speed must be decreased. For example, CDR with a width of 345 μm can be produced, while maintaining a low power (40 W) and a defocusing height z = 8 mm/∅ spot = 270 μm, and, to compensate, decrease the laser scanning speed to 10 mm/s (Fig. 5).

Higher defocusing heights were not sufficient to obtain properly consolidated CDR. It's worth noting that micrographs of the widest one-piece CDR obtained already show very strong contrasts in sintering progress between the centre and periphery of the CDR, and that significant cracks (longitudinal, i.e. parallel to the lasering line) are also observed (Fig. 5).

3.2.2. Ceramic anchored ribbons (CAR)

In a second phase, using similar investigative methods, we concentrated on CAR samples obtained for scanning speeds of less than 15 mm/s). Two focal heights z = 0 mm/∅ spot = 40 μm and z = 6 mm/∅ spot = 200 μm were considered. Also, for these two heights, various lasing speeds in between s = 0.6 (with a power equal to 40 W) and s = 10 mm/s (with a bit higher power of 48 W) were compared. The SEM micrographs of the six considered samples are reported in Fig. 6.

Observation of the various CAR samples reveals morphologies that differ from those of the CDR. A cross-sectional SEM of the CARs all show a densification gradient from the core to the edges of the lasered zone. Defocusing does indeed widen the CARs with a width of around 50 μm when z = 0/∅ spot = 40 μm and around 100 μm for z = 6 mm/∅ spot = 200 μm. Surprisingly, as laser scanning speed increases (particularly for the series of 4 samples with z = 6 mm/∅ spot = 200 μm), the density of the CAR obtained decreases, but the phenomenon of cracking increases. No doubt due to the anchoring of the film to the substrate, the volume contraction associated with sintering creates stresses that can be released, without crack formation, when speeds (and therefore temporal thermal gradients) remain relatively low, but produces crack propagation when speeds are higher. When defocusing is significantly increased until the widest possible lasered CARs are obtained, and this is combined with an increase in laser power so that the power per unit area received

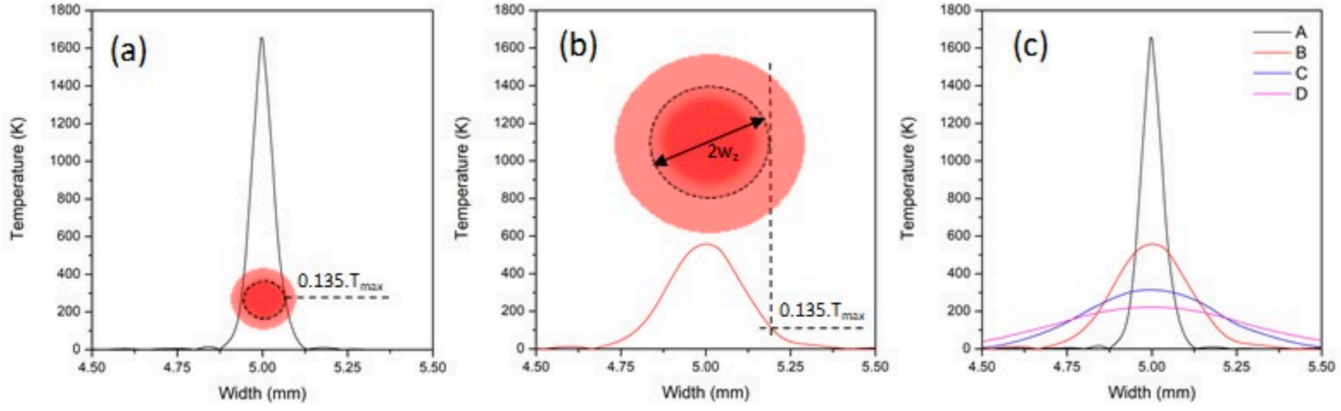

Fig. 3. Modelled temperature reached at the film surface with (a) a focalized laser beam, (b) a non-focalized laser beam (laser height position of 4 mm) and (c) comparison of the gaussian temperature distribution at the surface of the film for 4 laser height positions (A: z = 0 mm/∅ spot = 40 μm; B: z = 4 mm/∅ spot = 140 μm; C: z = 8 mm/∅ spot = 270 μm; D: z = 12 mm/∅ spot = 400 μm).

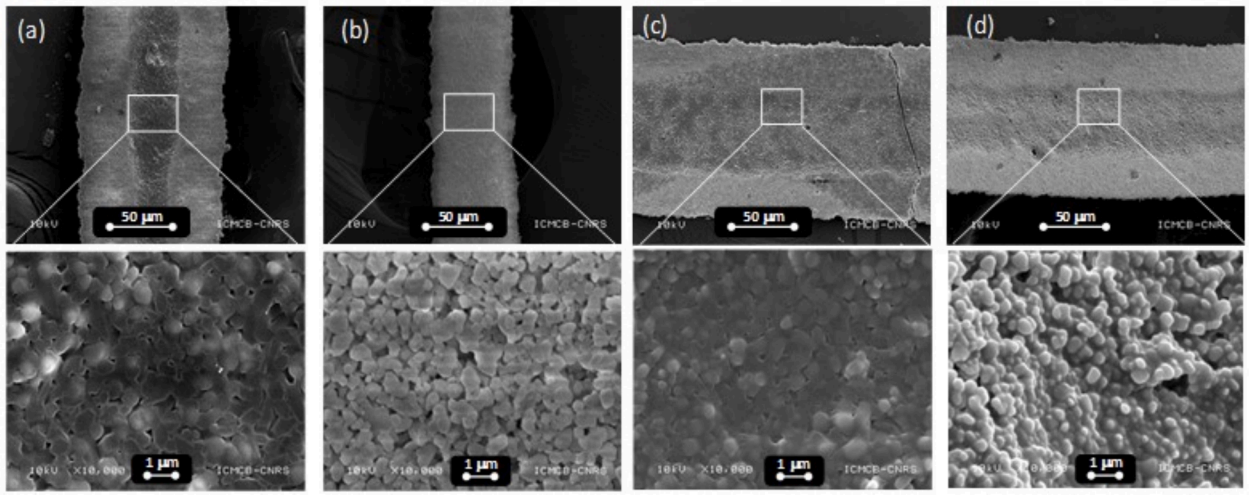

Fig. 4. SEM micrographs of CDR fabricated using (a) a laser scanning-speed s = 15 mm/s and (b) s = 40 mm/s for a focal height z = 0 mm/∅ spot = 40 µm and laser power P = 40 W; SEM micrographs of CDR fabricated using (c) a laser scanning-speed: s = 40 mm/s and (d) s = 60 mm/s for a focal height z = 6 mm/∅ spot = 200 µm and laser power P = 48 W.

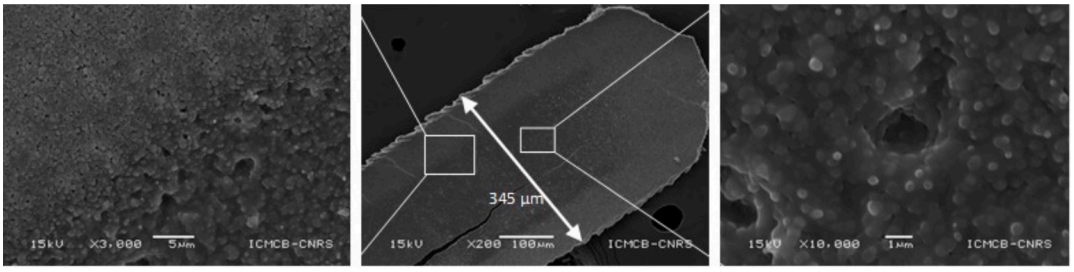

Fig. 5. (a) The largest CDR obtained (with a focal height z = 8 mm/∅ spot = 270 µm, a laser power P = 40 W and laser scanning-speed s = 10 mm/s).

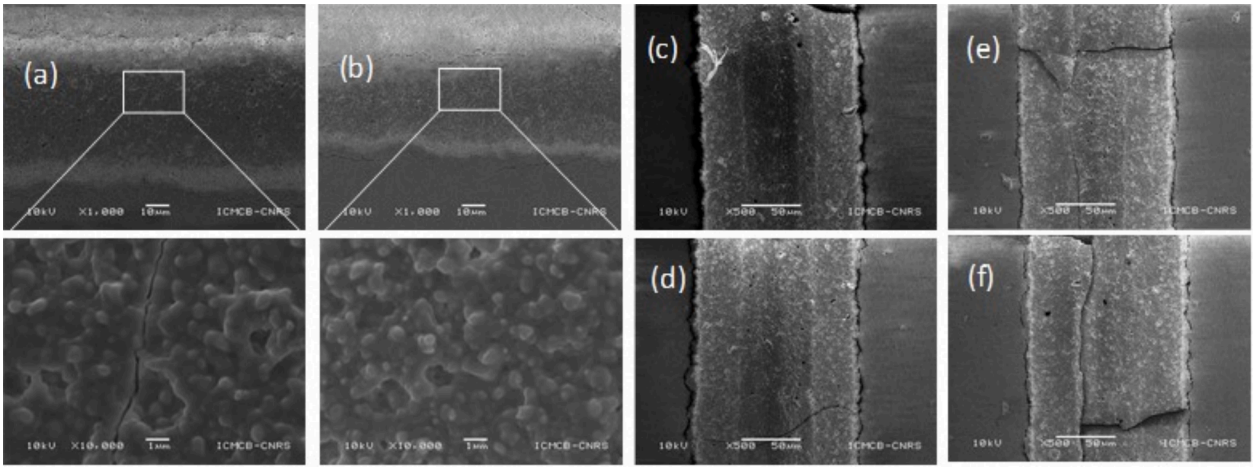

Fig. 6. SEM micrographs of CAR using (a) a laser scanning-speed s = 0.6 mm/s and (b) s = 2 mm/s for a focal height z = 0 mm/∅ spot = 40 µm and laser power P = 40 W; and using (c) s = 7 mm/s (d) s = 8 mm/s, (e) s = 9 mm/s, (f) = 10 mm/s for a focal height z = 6 mm/∅ spot = 200 µm and laser power P = 48 W.

by the lasered zones remains of the same order, anchored but cracked CARs with a highly reproducible and distinctive morphology can be obtained (Fig. 7). This morphology, which presents a succession of "petals", has already been observed in the literature on Zr-based metallic glasses subjected to the laser application [55]. However, this article suffers from proposing petals "upside down" compared to ours, i.e. the orientation of the petals is proposed as reversed with respect to the laser scanning direction compared to what is observed on our ceramic films. The origin of these differences may lie in the large differences between metallic materials and a ceramic as HAp. More broadly, patterning a ceramic alloy, glass or oxide surface has a variety of applications, including the creation of physical coloration [56,57], cytocompatibility [58] or even control of surface wettability [59].

Basing on the temperature gradient which can be stimulated thanks to FlexPDE software (Fig. 8**a**) it appears clearly that the crack propagation follows a route perpendicular to the isotherm lines, i.e. parallel to the temperature gradients (Fig. 8**b**). Following this idea, an attempt of schematization of the petal patterning is proposed (Fig. 8**c**).

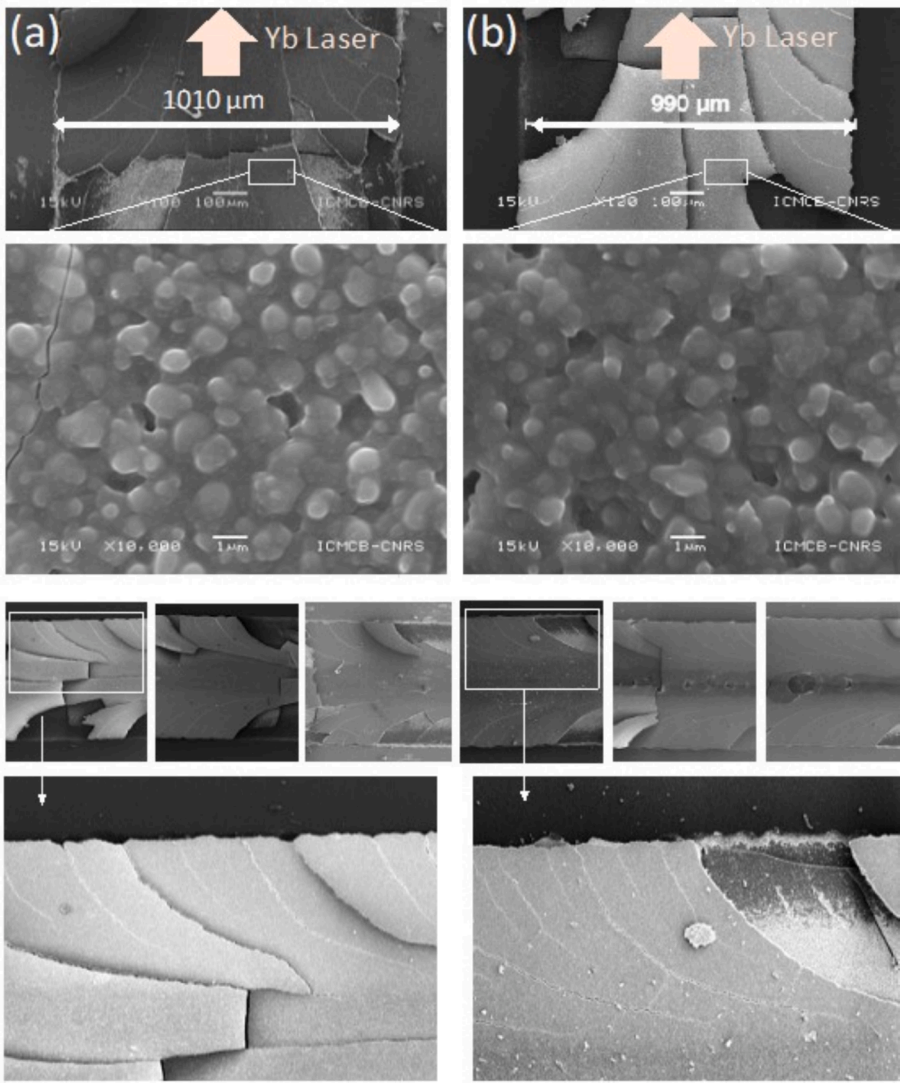

Fig. 7. (a) SEM micrographs of chipped CARs using (a) a laser scanning-speed s = 10 mm/s and (b) a scanning-speed s = 15 mm/s for a focal height z = 14 mm/∅ spot = 470 µm and laser power P = 88 W (pictures from upper level). Six different chipped CARs (with a focus on two of them) using different scanning speeds and/or powers with focal height z = 14 mm/∅ spot = 470 µm showing the regularity of the chipped patterns.

The schematic diagram of the vein-like structures forming the petal patterns is shown at different times versus laser propagation. Two basic ideas were integrated for creating the patterning scheme: (i) once the crack has appeared, its propagation follows a route parallel to the thermal gradients leading to arch-shaped crack lines; (ii) the constant periodic length between two successive cracks is in close relation to the constrains which cannot be elastically released and so, from the arch shape of the cracks, primary (as large black lines), secondary (dark blue lines) and even tertiary (pale blue lines) networks of cracks concomitantly appear.

The final studies in this publication focuses on analysing the effects of irradiating a powder bed through the thickness of the lasered lines (through depth), in order to explain in particular why CDRs are observed detached from the substrate, or CARs remain on the substrate.

3.3. *Effects of irradiation in depth*

3.3.1. *Ceramic delaminated ribbons (CDR)*

Cross-sections of CDR obtained with various laser scanning speeds are reported in Fig. 9.

In all cases, deep sintering progresses in such a way that the upper part of the CDR (surface subjected to laser irradiation) is very dense (with a columnar morphology) compared to the lower part of the CDR (initially bonded to the glass substrate). In other words, there is a strong density gradient between the top and bottom surfaces of CDR. Hence, the origin of the mechanical stresses producing delaminated and curled CDR becomes clear. It should also be noted that as laser scanning speed increases (associated with a reduction in the energy received by the film), lasered line become less dense overall, and therefore logically thicker. Using the "Mie Scatterring" software [60], it is interesting to simulate the laser absorption depth within the powder films in order to explain the strong density gradient observed (Fig. 10).

Refractive index and average particle size of the Cu-doped powder as well as the porosity percentage are the three parameters to input for this modelling calculation. The powder bed density is defined to 50 %, the two other parameters were adjusted. Calculations were made for a single wavelength of 1070 nm (the laser source wavelength). Regarding Fig. 10**a**, the refractive index, mainly controlled by its imaginary part related to the absorption coefficient, which we varied from 10 to 30 % with regard to the diffuse reflection spectra of our powders [46,47], has a very limited impact on the penetration depth profiles of the laser beam in HAp films. On the other hand, particle size (which in our case is about half a micron) has a significant impact (Fig. 10**b**). In any case, it's clear that with the size of the HAp grains in our films, and considering films

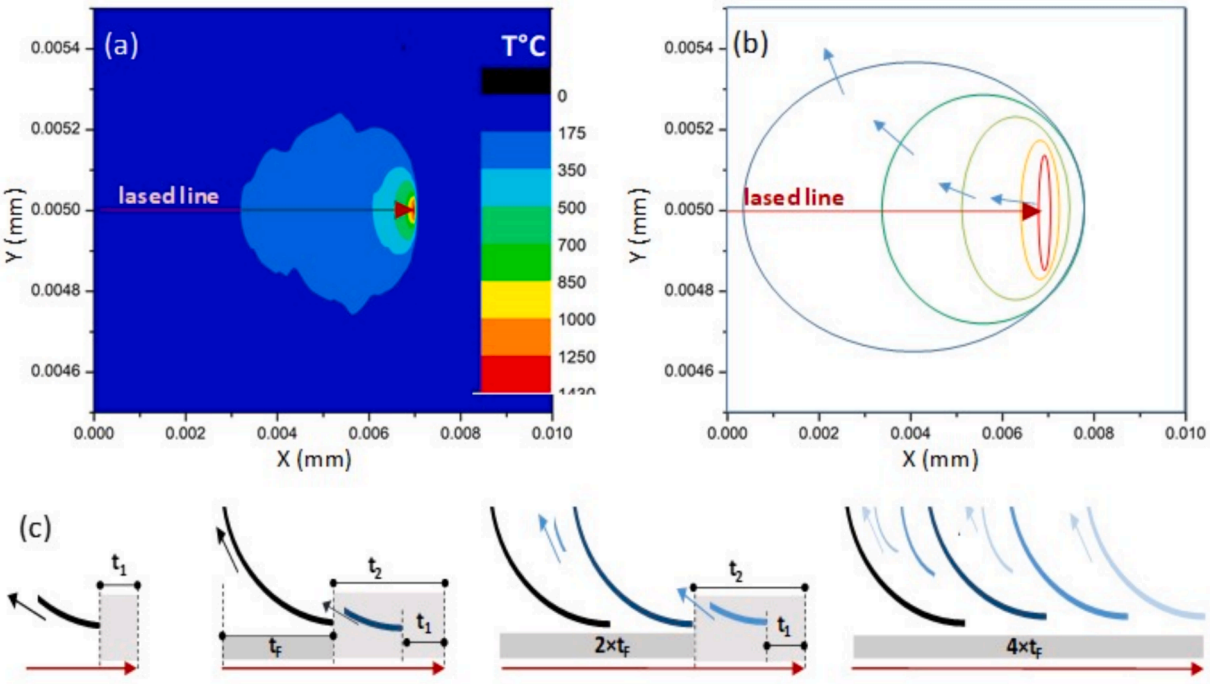

Fig. 8. (a) Modelled surface temperatures reached during lasing (with focal height z = 0 mm/∅ spot = 40 μm, laser power P = 40 W and s = 10 mm/s) and (b) a simplified scheme of the temperature levels with temperature gradients. (c) Decomposition in different schemes associated to different advancements of the laser scanning explaining the formation of the surface petal patterns (t_1, t_2 and t_F are arbitrary times).

around twenty microns thick, the laser beam has a penetration profile that fades significantly between the front and back surfaces of the films. The Mie scattering limitation of the laser beam within the films is therefore at the origin of the strong surface-core temperature gradient of the HAp films. Thermal gradient leads to the density gradients observed in depth of films, and thus to the detachment of CDRs due to the mechanical stresses then produced.

3.3.2. *Ceramic anchored ribbons (CAR)*

Then SEM cross-section views on various CARs are reported in Fig. 11. On CARs are produced thanks to higher irradiation energy, it could be supposed that the temperature has been raised to sufficiently high values at the surface for the entire film thickness to be highly densified by thermal conductivity. In fact, the bonding of the films to the substrate can be explained by welding caused by a sharp rise in temperature at the film/substrate interface. There is some evidence of this, but the phenomenon observed is more complex. CARs are obtained when the entire film thickness is not perfectly densified. It appears that cross-sectional views of the films show a sandwich morphology, with a distinctly dense upper part, a more porous intermediate layer, and a lower part "bonded" to the substrate that is once again denser. Films obtained with parameters at the boundary between obtaining CARs and CDRs, show the beginning of film detachment with absence of densification at the interface, demonstrating the switchable character of this set of parameters. Film adhesion is related to a sufficient temperature rise at the film/substrate interface to cause co-sintering of film and substrate at this interface. However, the existence of a more porous intermediate layer seems to demonstrate that beyond thermal conduction causing a monotonically decreasing gradient between the top surface and the film/substrate interface, a wall effect allowing an accumulation of energy at this interface seems to occur. FlexPDE software was used to model this wall effect (Fig. 12). Firstly, as our FlexPDE simulations here are only able to give the surface temperatures of an irradiated film (working in 2 dimensions), we arranged to meet our phenomenological observation by simulating laser irradiation on a two-phase material with an interface orthogonal to the surface of the composite material created. The parameters required for the simulation, characterizing the glass phase and the Cu-doped HAp phase, were implemented in line with our Cu-doped HAp layers deposited on an amorphous silicate slide (in terms of heat capacity, absorption coefficient, thermal conductivity, etc.). The temperature levels predicted using thermal simulation show very clearly that the creation of an interface close to the lasered line (the interface was positioned at 50 and 100 μm from the lasered line of passage, with coordinate Y = 0, Fig. 12**b and c**)) produce a very strong wall effect, leading to highly asymmetrical temperature levels perpendicular to the lasered line. Temperatures on the side with the interface created are much higher than those on the side without (for the same distance from the center of the lasered line). The result is evidenced for an interface located at a distance of 50 μm. The effects fade rapidly and is already very softened for a distance of 100 μm.

Thus, several complex and interrelated phenomena take place concomitantly during laser radiation of Cu-doped HAp powder films. The transferred laser beam is spread out (Mie scattering type) but does not penetrate the entire thickness of the film, also no interaction takes place between the radiation and the silicate substrate. This radiation, partially absorbed by the chromophore (copper) doping the HAp structure, produces strong local heating, the intensity of which depends on a number of parameters, including laser power, scanning speed and focus. The heating is accompanied by a significant rise in film temperature, well beyond the irradiated volume, due to the phenomenon of thermal conductivity. The substrate also acts as a wall, "concentrating" the heat at the film-substrate interface. So, depending on the energy received, two main types of ribbons can be produced by lasering a single centimetre-long line.

Firstly, CDRs with a dense crust on the surface, more porous below this crust, with no sintering yet marked at the film/substrate interface are discussed (**graphical abstract, left side**). For this first type of ribbon, the energy concentration gradient will cause the ribbon to lift off (by curling concavely). One-dimensional, mechanically coherent (which can be manipulated) objects can be produced with some control over their width (via laser focusing) and thickness (via the thickness of the lasered film). Secondly, CARs (**graphical abstract, right side**) typically

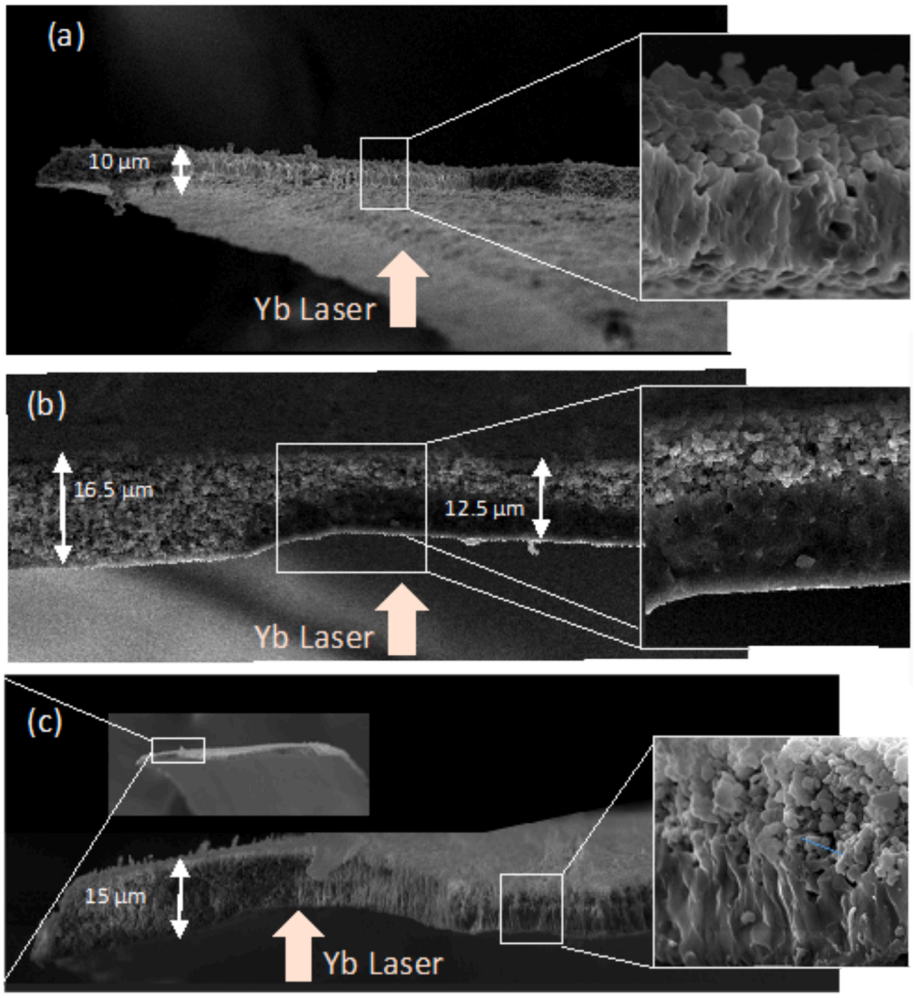

Fig. 9. SEM micrographs (cross section views) of three different CDR obtained with a focal height z = 8 mm/Ø spot = 270 µm, a laser power P = 40 W and laser scanning speeds (a) s = 7 mm/s, (b) s = 8 mm/s and (c) c = 10 mm/s.

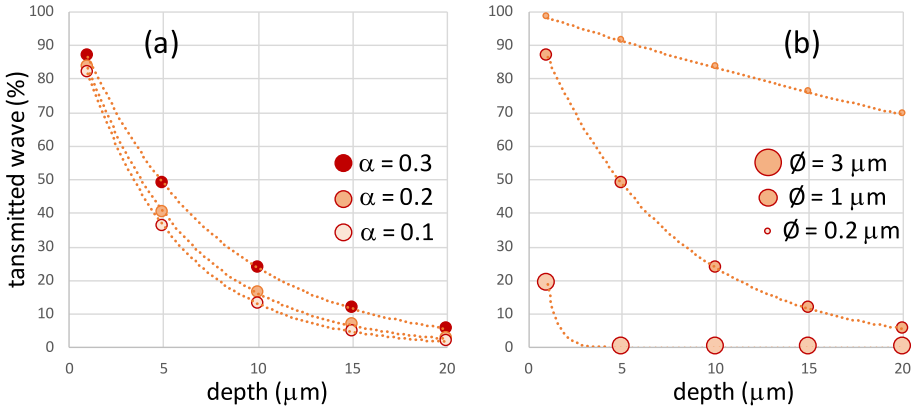

Fig. 10. Laser transmission percentage versus transmitted medium depth for a laser beam light with 1070 nm wavelength, considering the transmission medium made of a pack (50 % density) of spherical Cu-doped HAP particles with (a) a fixed diameter Ø = 1 µm and various absorption coefficients and (b) a defined absorption coefficient α = 0.2 (20 %) and various particles diameters.

feature a sandwich-like architecture in their thickness, with a dense surface crust, a more porous intermediate zone and a lower zone (approaching the glassy substrate) that is denser again.

By controlling the material and laser parameters, powder bed laser consolidation can be used to produce very finely controlled structures, even on refractory ceramic materials with very high melting points.

4. Conclusion

Thanks to the copper ions incorporated into the hydroxyapatite matrix and so the absorption of a high-power laser (1070 µm), Cu-doped HAp thin powder bed deposited on a transparent silicate lime substrate can be sintered thanks to heating from powder bed laser sintering.

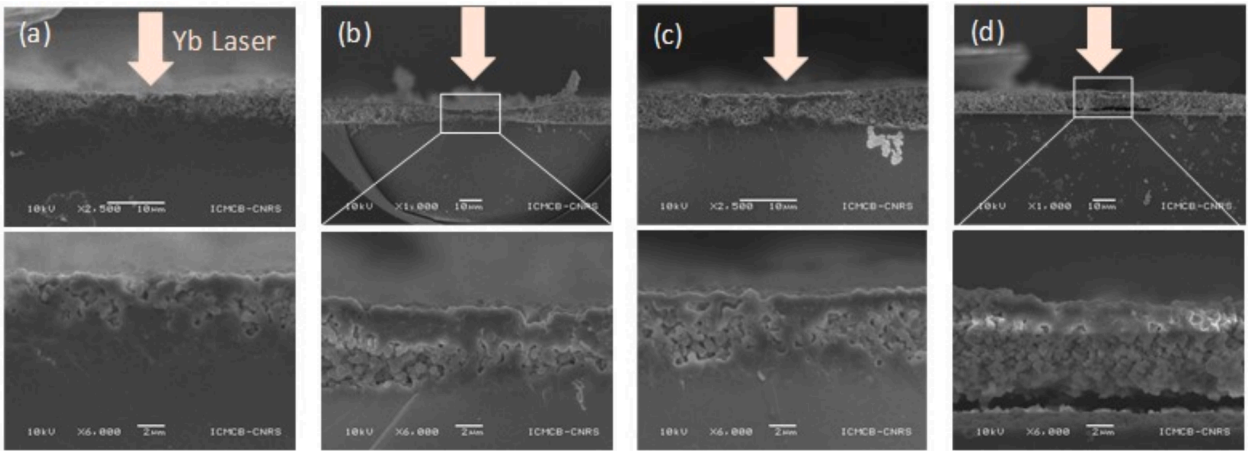

Fig. 11. SEM micrographs (cross section views) of CAR using for a focal height z = 0 mm/∅ spot = 40 μm and laser power P = 40 W and laser scanning speeds (a) s = 0.6 mm/s, (b) s = 2 mm/s; (c) s = 4 mm/s and (d) s = 6 mm/s.

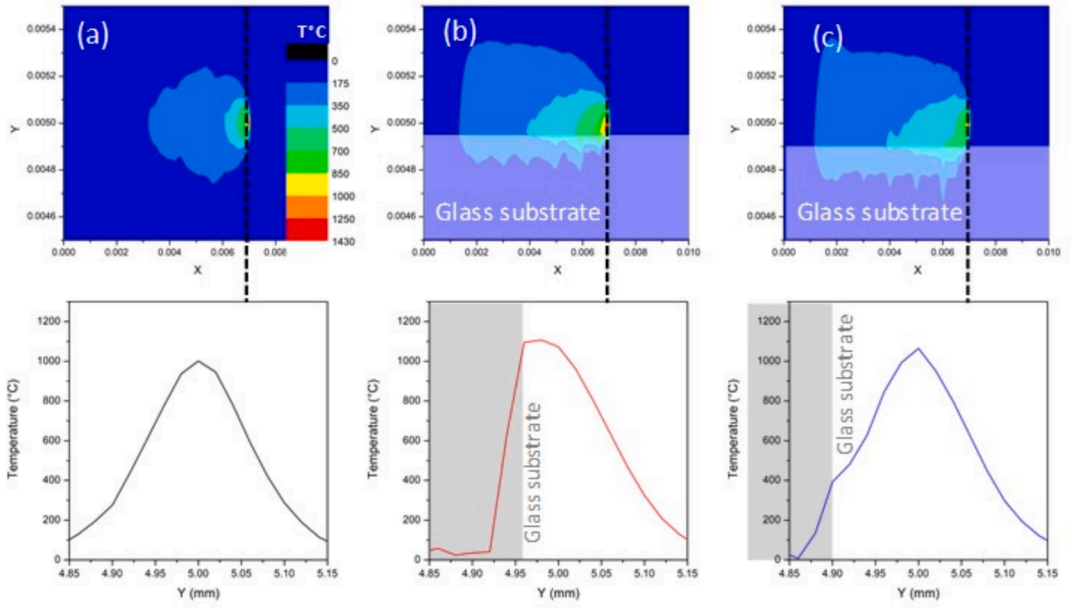

Fig. 12. Modelled surface temperatures reached during lasing (with focal height /∅ spot = 0 mm /40 μm, laser power P = 40 W and s = 10 mm/s), (a) without any wall effect, with a created infinite interface HAP-film / silicate glass parallel to the lasered line (b) at 50 μm of the lasered line center and (c) at 100 mm of the lasered line center.

Herein, detailed investigation at the micrometer scale, combining SEM observations and thermal modelling (using FlexPDE software) has allowed to better understand and control the thermal processes occurring in the powder bed when lasered along a centimeter line. Especially, the impact of various laser parameters: as power, scanning speed, laser focusing, were carefully analyzed. Two types of ceramic ribbons can be produced: delaminated ceramic ribbons (CDR) or anchored ceramic ribbons (CAR). SEM analysis revealed surface density gradients in both ribbon types, with density decreasing from center to edge, but maintaining distinct ribbon boundaries. The porous powder bed causes Mie scattering of the laser beam, resulting in rapid intensity reduction with increasing penetration depth. Mechanical stresses cause the detachment and curled shape of CDRs, which are useful as building blocks for bone scaffolds through stacking. CARs also show density gradients but feature a sandwich structure with a low-density middle layer between two high-density layers. The sandwich structure in CARs results from Mie scattering and the thermal barrier effect at the film-substrate interface. CARs exhibit petal-like crack networks, likely propagating perpendicular to isothermal lines, as suggested by thermal modeling.

CRediT authorship contribution statement

François Rouzé l'Alzit: Methodology, Investigation, Formal analysis. **Benoit Glorieux:** Writing – review & editing, Formal analysis. **Thierry Cardinal:** Writing – review & editing, Methodology, Conceptualization. **Manuel Gaudon:** Supervision, Conceptualization.

Declaration of competing interest

The authors declare the following financial interests/personal relationships which may be considered as potential competing interests: [Manuel GAUDON reports financial support was provided by University of Bordeaux, France. Manuel gaudon reports a relationship with University of Bordeaux, France that includes: employment. If there are other authors, they declare that they have no known competing financial interests or personal relationships that could have appeared to influence

the work reported in this paper].

Data availability

No data was used for the research described in the article.

References

[1] N. Eliaz, N. Metoki, Calcium phosphate bioceramics: a review of their history, structure, properties, Coating Technologies and Biomedical Applications. Materials 10 (2017) 334, https://doi.org/10.3390/ma10040334.

[2] S.V. Dorozhkin, Bioceramics of calcium orthophosphates, Biomaterials 31 (2010) 1465–1485, https://doi.org/10.1016/j.biomaterials.2009.11.050.

[3] S. Catros, F. Guillemot, E. Lebraud, C. Chanseau, S. Perez, R. Bareille, et al., Physico-chemical and biological properties of a nano-hydroxyapatite powder synthesized at room temperature, IRBM 31 (2010) 226–233, https://doi.org/10.1016/j.irbm.2010.04.002.

[4] J.N. DiNoro, N.C. Paxton, J. Skewes, Z. Yue, P.M. Lewis, R.G. Thompson, et al., Laser sintering approaches for bone tissue engineering, Polymers 14 (2022) 2336, https://doi.org/10.3390/polym14122336.

[5] J.T.B. Ratnayake, M. Mucalo, G.J. Dias, Substituted hydroxyapatites for bone regeneration: a review of current trends, J. Biomed. Mater. Res. B Appl. Biomater. 105 (2017) 1285–1299, https://doi.org/10.1002/jbm.b.33651.

[6] M. Lasgorceix, E. Champion, T. Chartier, Shaping by microstereolithography and sintering of macro–micro-porous silicon substituted hydroxyapatite, J. Eur. Ceram. Soc. 36 (2016) 1091–1101, https://doi.org/10.1016/j.jeurceramsoc.2015.11.020.

[7] M. Šupová, Substituted hydroxyapatites for biomedical applications: a review, Ceram. Int. 41 (2015) 9203–9231, https://doi.org/10.1016/j.ceramint.2015.03.316.

[8] Bose S. 2013 Understanding of dopant-induced osteogenesis and angiogenesis in calcium phosphate ceramics 31 12. doi: 10.1016/j.tibtech.2013.06.005.

[9] R.B. Unabia, S. Bonebeau, R.T. Candidato, L. Pawłowski, Preliminary study on copper-doped hydroxyapatite coatings obtained using solution precursor plasma spray process, Surf. Coat. Technol. 353 (2018) 370–377, https://doi.org/10.1016/j.surfcoat.2018.09.008.

[10] Y. Huang, X. Zhang, R. Zhao, H. Mao, Y. Yan, X. Pang, Antibacterial efficacy, corrosion resistance, and cytotoxicity studies of copper-substituted carbonated hydroxyapatite coating on titanium substrate, J. Mater. Sci. 50 (2015) 1688–1700, https://doi.org/10.1007/s10853-014-8730-1.

[11] F. Rengier, A. Mehndiratta, H. von Tengg-Kobligk, C.M. Zechmann, R. Unterhinninghofen, H.-U. Kauczor, et al., 3D printing based on imaging data: review of medical applications, Int J CARS 5 (2010) 335–341, https://doi.org/10.1007/s11548-010-0476-x.

[12] N.K. Vail, L.D. Swain, W.C. Fox, T.B. Aufdlemorte, G. Lee, J.W. Barlow, Materials for biomedical applications, Mater. Des. 20 (1999) 123–132, https://doi.org/10.1016/S0261-3069(99)00018-7.

[13] F. Edith Wiria, N. Sudarmadji, K. Fai Leong, C. Kai Chua, E. Wei Chng, C.C. Chai, Selective laser sintering adaptation tools for cost effective fabrication of biomedical prototypes, Rapid Prototyp. J. 16 (2010) 90–99, https://doi.org/10.1108/13552541011025816.

[14] B. Duan, M. Wang, Selective laser sintering and its application in biomedical engineering, MRS Bull. 36 (2011) 998–1005, https://doi.org/10.1557/mrs.2011.270.

[15] A. Mazzoli, Selective laser sintering in biomedical engineering, Med. Biol. Eng. Compu. 51 (2013) 245–256, https://doi.org/10.1007/s11517-012-1001-x.

[16] S.F.S. Shirazi, S. Gharehkhani, M. Mehrali, H. Yarmand, H.S.C. Metselaar, N. Adib Kadri, et al., A review on powder-based additive manufacturing for tissue engineering: selective laser sintering and inkjet 3D printing, Sci. Technol. Adv. Mater. 16 (2015) 033502, https://doi.org/10.1088/1468-6996/16/3/033502.

[17] E. Champion, A. Magnaudeix, P. Pascaud-Mathieu, T. Chartier, 14 - Advanced processing techniques for customized ceramic medical devices, Advances in Ceramic Biomaterials, Elsevier Ltd (2017) 433–468.

[18] N. Travitzky, A. Bonet, B. Dermeik, T. Fey, I. Filbert-Demut, L. Schlier, et al., Additive manufacturing of ceramic-based materials, Adv. Eng. Mater. 16 (2014) 729–754, https://doi.org/10.1002/adem.201400097.

[19] Z. Chen, Z. Li, J. Li, C. Liu, C. Lao, Y. Fu, et al., 3D printing of ceramics: a review, J. Eur. Ceram. Soc. 39 (2019) 661–687, https://doi.org/10.1016/j.jeurceramsoc.2018.11.013.

[20] I. Denry, J.R. Kelly, Emerging ceramic-based materials for dentistry, J. Dent. Res. 93 (2014) 1235–1242, https://doi.org/10.1177/0022034514553627.

[21] M. Salmi, Additive manufacturing processes in medical applications, Materials 14 (2021) 191, https://doi.org/10.3390/ma14010191.

[22] P. Rider, Ž.P. Kačarević, S. Alkildani, S. Retnasingh, R. Schnettler, M. Barbeck, Additive manufacturing for guided bone regeneration: a perspective for alveolar ridge augmentation, Int. J. Mol. Sci. 19 (2018) 3308, https://doi.org/10.3390/ijms19113308.

[23] L. Ferrage, G. Bertrand, P. Lenormand, D. Grossin, B. Ben-Nissan, A review of the additive manufacturing (3DP) of bioceramics: alumina, zirconia (PSZ) and hydroxyapatite, J. Aust. Ceram. Soc. 53 (2017) 11–20, https://doi.org/10.1007/s41779-016-0003-9.

[24] R. Galante, C.G. Figueiredo-Pina, A.P. Serro, Additive manufacturing of ceramics for dental applications: a review, Dent. Mater. 35 (2019) 825–846, https://doi.org/10.1016/j.dental.2019.02.026.

[25] R. Shanthar, K. Chen, C. Abeykoon, Powder-based additive manufacturing: a critical review of materials, methods, opportunities, and challenges, Adv. Eng. Mater. 25 (2023) 2300375, https://doi.org/10.1002/adem.202300375.

[26] S. Chaudhary, S.K. Avinashi, J. Rao, C. Gautam, Recent advances in additive manufacturing, applications and challenges for dentistry: a review, ACS Biomater Sci. Eng. 9 (2023) 3987–4019, https://doi.org/10.1021/acsbiomaterials.2c01561.

[27] A.U. Rehman, P. Navarrete-Segado, M.U. Salamci, C. Frances, M. Tourbin, D. Grossin, Understanding the consolidation mechanism of selective laser sintering/powder bed selective laser process of ceramics: hydroxyapatite case, Rapid Prototyp. J. 30 (2024) 677–695, https://doi.org/10.1108/RPJ-04-2023-0128.

[28] Yadroitsev I, Bertrand Ph, Smurov I. 2007 Parametric analysis of the selective laser melting process. Applied Surface Science. 253 8064–9. doi: 10.1016/j.apsusc.2007.02.088.

[29] D. Grossin, A. Montón, P. Navarrete-Segado, E. Özmen, G. Urruth, F. Maury, et al., A review of additive manufacturing of ceramics by powder bed selective laser processing (sintering / melting): calcium phosphate, silicon carbide, zirconia, alumina, and their composites, Open Ceram. 5 (2021) 100073, https://doi.org/10.1016/j.oceram.2021.100073.

[30] C. Shuai, P. Li, J. Liu, S. Peng, Optimization of TCP/HAP ratio for better properties of calcium phosphate scaffold via selective laser sintering, Mater Charact 77 (2013) 23–31, https://doi.org/10.1016/j.matchar.2012.12.009.

[31] C. Shuai, J. Zhuang, H. Hu, S. Peng, D. Liu, J. Liu, In vitro bioactivity and degradability of β-tricalcium phosphate porous scaffold fabricated via selective laser sintering, Biotechnol. Appl. Biochem. 60 (2013) 266–273, https://doi.org/10.1002/bab.1064.

[32] D. Liu, J. Zhuang, C. Shuai, S. Peng, Mechanical properties\textquotesingle improvement of a tricalcium phosphate scaffold with poly-l-lactic acid in selective laser sintering, Biofabrication 5 (2013) 025005, https://doi.org/10.1088/1758-5082/5/2/025005.

[33] C. Gao, B. Yang, H. Hu, J. Liu, C. Shuai, S. Peng, Enhanced sintering ability of biphasic calcium phosphate by polymers used for bone scaffold fabrication, Mater. Sci. Eng. C 33 (2013) 3802–3810, https://doi.org/10.1016/j.msec.2013.05.017.

[34] K.H. Tan, C.K. Chua, K.F. Leong, C.M. Cheah, P. Cheang, M.S. Abu Bakar, et al., Scaffold development using selective laser sintering of polyetheretherketone–hydroxyapatite biocomposite blends, Biomaterials 24 (2003) 3115–3123, https://doi.org/10.1016/S0142-9612(03)00131-5.

[35] Y. Zhang, L. Hao, M.M. Savalani, R.A. Harris, L.D. Silvio, K.E. Tanner, In vitro biocompatibility of hydroxyapatite-reinforced polymeric composites manufactured by selective laser sintering, J. Biomed. Mater. Res. A 91A (2009) 1018–1027, https://doi.org/10.1002/jbm.a.32298.

[36] T. Kumaresan, R. Gandhinathan, M. Ramu, M. Ananthasubramanian, K. B. Pradheepa, Design, analysis and fabrication of polyamide/ hydroxyapatite porous structured scaffold using selective laser sintering method for bio-medical applications, J. Mech. Sci. Technol. 30 (2016) 5305–5312, https://doi.org/10.1007/s12206-016-1049-x.

[37] F. Dabbas, S.L. Stares, J.M. Mascheroni, D. Hotza, G.V. Salmoria, et al., in: Selective Laser Sintering of Polyamide/hydroxyapatite Scaffolds, Springer International Publishing, Cham, 2017, pp. 95–103.

[38] J.M. Williams, A. Adewunmi, R.M. Schek, C.L. Flanagan, P.H. Krebsbach, S. E. Feinberg, et al., Bone tissue engineering using polycaprolactone scaffolds fabricated via selective laser sintering, Biomaterials 26 (2005) 4817–4827, https://doi.org/10.1016/j.biomaterials.2004.11.057.

[39] S. Eosoly, D. Brabazon, S. Lohfeld, L. Looney, Selective laser sintering of hydroxyapatite/poly-ε-caprolactone scaffolds, Acta Biomater. 6 (2010) 2511–2517, https://doi.org/10.1016/j.actbio.2009.07.018.

[40] Ph. Bertrand, F. Bayle, C. Combe, P. Goeuriot, I. Smurov, Ceramic components manufacturing by selective laser sintering, Appl. Surf. Sci. 254 (2007) 989–992, https://doi.org/10.1016/j.apsusc.2007.08.085.

[41] C. Shuai, Y. Nie, C. Gao, P. Feng, J. Zhuang, Y. Zhou, et al., The microstructure evolution of nanohydroxapatite powder sintered for bone tissue engineering, J. Exp. Nanosci. 8 (2013) 762–773, https://doi.org/10.1080/17458080.2011.606507.

[42] C. Shuai, C. Gao, Y. Nie, H. Hu, Y. Zhou, S. Peng, Structure and properties of nano-hydroxypatite scaffolds for bone tissue engineering with a selective laser sintering system, Nanotechnology 22 (2011) 285703, https://doi.org/10.1088/0957-4484/22/28/285703.

[43] C. Shuai, P. Feng, C. Cao, S. Peng, Processing and characterization of laser sintered hydroxyapatite scaffold for tissue engineering, Biotechnol Bioproc E 18 (2013) 520–527, https://doi.org/10.1007/s12257-012-0508-1.

[44] A.D. Anastasiou, C.L. Thomson, S.A. Hussain, T.J. Edwards, S. Strafford, M. Malinowski, et al., Sintering of calcium phosphates with a femtosecond pulsed laser for hard tissue engineering, Mater. Des. 101 (2016) 346–354, https://doi.org/10.1016/j.matdes.2016.03.159.

[45] T. Bazin, F. Rouzé-l'Alzit, A. Demourgues, I. Julien, C. Bertrand, S. Catros, et al., Ceramic Powder Bed Laser Sintering (CPBLS) on copper-doped hydroxyapatite: creation of thin (5–50 μm thick) consolidated ceramic patterns, Ceram. Int. 47 (2021) 18565–18574, https://doi.org/10.1016/j.ceramint.2021.03.182.

[46] F. Rouzé l'Alzit, T. Bazin, T. Cardinal, U-C. Chung, S. Catros, C. Bertrand, et al., Powder bed laser sintering of copper-doped hydroxyapatite: numerical and experimental parametric analysis, Addit. Manuf. (2021) 102044, https://doi.org/10.1016/j.addma.2021.102044.

[47] S. Das, Physical aspects of process control in selective laser sintering of metals, Adv. Eng. Mater. 5 (2003) 701–711, https://doi.org/10.1002/adem.200310099.

[48] V.E. Beal, R.A. Paggi, G.V. Salmoria, A. Lago, Statistical evaluation of laser energy density effect on mechanical properties of polyamide parts manufactured by

selective laser sintering, J. Appl. Polym. Sci. 113 (2009) 2910–2919, https://doi.org/10.1002/app.30329.
[49] A. Bahador, E. Hamzah, K. Kondoh, T. Abubakar, F. Yusof, S.N. Saud, et al., Defocusing effects of laser beam on the weldability of powder metallurgy Ti-based shape memory alloys, Procedia Eng. 184 (2017) 205–213, https://doi.org/10.1016/j.proeng.2017.04.087.
[50] S. Khademzadeh, N. Parvin, P.F. Bariani, F. Mazzucato, Effects of micro laser sintering process parameters on quality of nickel-titanium single tracks and thin walls, Met. Mater. Int. 21 (2015) 1081–1090, https://doi.org/10.1007/s12540-015-5304-y.
[51] F. Lambiase, S. Genna, Homogenization of temperature distribution at metal-polymer interface during Laser Direct Joining, Opt. Laser Technol. 128 (2020) 106226, https://doi.org/10.1016/j.optlastec.2020.106226.
[52] F. Rouzé l'Alzit, T. Cardinal, GL. Vignoles, É. Bonnet, M. Gaudon, Thermal history mapping in powder bed laser sintering at the micrometer scale, ACS Omega (2022), https://doi.org/10.1021/acsomega.2c04683.
[53] N. Kamboj, A. Ressler, I. Hussainova, Bioactive ceramic scaffolds for bone tissue engineering by powder bed selective laser processing: a review, Materials 14 (2021) 5338, https://doi.org/10.3390/ma14185338.
[54] M. Shehryar Khan, S.I. Shahabad, M. Yavuz, W.W. Duley, E. Biro, Y. Zhou, Numerical modelling and experimental validation of the effect of laser beam defocusing on process optimization during fiber laser welding of automotive press-hardened steels, J. Manuf. Process. 67 (2021) 535–544, https://doi.org/10.1016/j.jmapro.2021.05.006.
[55] Y. Qian, H. Huang, C. Wang, P. Yu, J. Xu, Z. Zhang, Formation of leaf-shaped microstructure on Zr-based metallic glass via nanosecond pulsed laser irradiation, J. Manuf. Process. 72 (2021) 61–70, https://doi.org/10.1016/j.jmapro.2021.10.016.
[56] Q. Gao, D. Ouyang, X. Liu, S. Wu, X. Huang, N. Li, Fabricating colorful bulk metallic glass surfaces by femtosecond laser processing, Mater. Chem. Phys. 266 (2021) 124561, https://doi.org/10.1016/j.matchemphys.2021.124561.
[57] H. Zhang, Y. Qian, L. Zhang, D. Zhang, H. Liu, H. Huang, Surface coloration of Zr-based metallic glass by nanosecond pulsed laser irradiation in ambient atmosphere, Mater. Lett. 304 (2021) 130721, https://doi.org/10.1016/j.matlet.2021.130721.
[58] J. Schroers, T. Nguyen, S. O'Keeffe, A. Desai, Thermoplastic forming of bulk metallic glass—applications for MEMS and microstructure fabrication, Mater. Sci. Eng. A 449–451 (2007) 898–902, https://doi.org/10.1016/j.msea.2006.02.398.
[59] Y. Jiao, E. Brousseau, X. Shen, X. Wang, Q. Han, H. Zhu, et al., Investigations in the fabrication of surface patterns for wettability modification on a Zr-based bulk metallic glass by nanosecond laser surface texturing, J. Mater. Process. Technol. 283 (2020) 116714, https://doi.org/10.1016/j.jmatprotec.2020.116714.
[60] S.L. Jacques, Optical properties of biological tissues: a review, Phys. Med. Biol. 58 (2013) 37. http://iopscience.iop.org/0031-9155/58/11/R37.